Spectroscopic characterization of prepulsed x-ray laser plasmas

M. Nantel,* A. Klisnick, G. Jamelot, P. B. Holden, B. Rus, A. Carillon, and P. Jaeglé
Laboratoire de Spectroscopie Atomique et Ionique, Bâtiment 350, Université de Paris–Sud, 91405 Orsay, France

Ph. Zeitoun† and G. Tallents
Department of Physics, University of Essex, Colchester CO 435Q, United Kingdom

A. G. MacPhee and C. L. S. Lewis
Department of Pure and Applied Physics, Queen's University of Belfast, Belfast BT7 INN, United Kingdom

S. Jacquemot and L. Bonnet
Commissariat à l'Energie Atomique, Centre d'Etudes de Limeil-Valenton, 94195 Villeneuve Saint-Georges Cedex, France
(Received 18 March 1996)

Through the use of time-integrated space-resolved keV spectroscopy, we investigate line plasmas showing gain in Ne-like nickel, copper, and zinc for irradiation using the prepulse technique. The experiments were conducted at 1.06 μm with the prepulse to main pulse intensity contrast ranging from 10^{-6} to 10^{-2}. The effect of the prepulses on the plasma conditions is inferred through spectroscopic line ratio diagnostics for the electron temperature, the Ne-like ground-state density, and the lateral size of the Ne-like region. It is observed that neither the value of the electronic temperature nor its spatially resolved profile along the linear focus axis varies significantly with the prepulse level, contrary to the lateral width and the density of the Ne-like region in the plasma, which are seen to increase. These results explain, at least in part, why prepulsed x-ray lasers show such high gain and brightness. [S1063-651X(96)10009-X]

PACS number(s): 52.25.−b, 07.85.−m, 42.55.Vc, 32.30.−r

I. INTRODUCTION

Much attention has been given recently to prepulsed x-ray lasers [1]. It has been shown in the past few years that low-level prepulses added to the plasma-creating pump laser pulse significantly enhance the performance of a wide range of collisionally excited Ne-like x-ray lasers [1–12]. Whereas the early investigations required small but still multijoule-level prepulses [2–5], more recent studies have successfully used subjoule-level prepulses at smaller laser facilities to critically improve the output intensity of their x-ray lasers [6–12]. It is believed that a prepulse creates a weakly ionized preplasma in front of the target before the arrival of the main pulse and that this preplasma plays an essential role in the laser-matter interaction [8,10–13]. One interesting feature of these results is that it is the $(1s^2 2s^2 2p^5)$ $3p$ J=0 to $3s$ $J=1$ transition (simply labeled hereafter $J=0-1$) that shows the most impressive improvement when prepulses are employed. One could argue that these recent developments have explained away the infamous ''$J=0-1$ anomaly'' [14]: the line finally displays the largest gain and becomes the dominant feature in the extreme-ultraviolet (XUV) spectra, as it was predicted in the early days of collisional pumping x-ray lasers [14,15]. Meanwhile, the two successful $3p$ $J=2$ to $3s$ $J=1$ lines (hereafter designated $J=2-1$) react very little to the addition of a prepulse [11,12]. This difference in behavior between the $J=0-1$ and $J=2-1$ lines and the fact that they are observed to be emitted at different distances from the target and with different time histories [4,16,17] suggest that the prepulse changes conditions in the plasma for which the $J=0-1$ line is more sensitive. In particularly, the neonlike ion density and the electron temperature directly control the main populating mechanism of the upper $J=0$ state: the monopole collisional excitation from the ground state $2p$ $J=0$ [15]. Also, because the population inversion occurs nearer the target, a key factor in the $J=0-1$ laser is the propagation of the amplified radiation, which is highly dependent on the size of the gain region, the density gradients, and the homogeneity of the plasma [18–22].

Most investigations of prepulsed x-ray lasers have been limited to the phenomenological observation of their performances under different prepulse conditions and to computer simulations [3,10,22–24]. In order to increase our understanding of prepulsed x-ray lasers, it is crucial to characterize the plasma and exhibit the dependence of the main hydrodynamical parameters on the prepulse level. Some efforts are now being directed to the study of the formation of the preplasma [25,26] and the lasing plasma itself [27], while others concentrate on identifying the location of the gain region and its shift with the prepulse level [10]. We present here a comprehensive and quantitative experimental characterization of x-ray laser plasmas created with prepulsed irradiation. In this paper we will present spectroscopic diagnostics for the electron temperature, the Ne-like ground-state density, and the Ne-like region lateral size, for zinc, copper, and nickel x-ray laser plasmas created with the Ecole Polytechnique LULI laser; we also compare these with preliminary

*Author to whom all correspondence should be sent. Present address: Center for Ultrafast Optical Science, University of Michigan, Ann Arbor, Michigan 48109-2099.

†Present address: Laboratoire de Spectroscopie Atomique et Ionique, Bâtiment 350, Université de Paris–Sud, 91405 Orsay, France.

results of CHIVAS-hydrodynamics–LASIX detailed kinetics–SPECTRA-radiative-transfer simulations [23,24].

II. EXPERIMENTAL SETUP

The experiments were performed at the Laboratoire pour l'Utilisation des Lasers Intenses (LULI) facility located at the Ecole Polytechnique in Palaiseau, France. The LULI laser is a Nd:glass laser operating at 1.06 μm with six beams delivering for our experiments a total of 325 ± 25 J on target, in 800 ± 50-ps full width at half maximum (FWHM) Gaussian pulses. The prepulses were obtained in two different ways. First, the main pulse can be preceded by a prepulse train, composed of about five (20–60)-mJ successive prepulses, separated by 10 ns (as illustrated in Ref. [11]). This temporal structure results from a normal leakage in the Pockel cell, which selects from the oscillator the main pulse to be amplified in the LULI chain. The ratio of the last prepulse to main pulse intensity is then of about 5×10^{-4} after the amplification. It is with this prepulse train that the saturated Ne-like Zn $J=0-1$ x-ray laser at 212 Å was obtained at LULI [7,16,17]. Alternatively, the prepulse train being eliminated by the addition of a second Pockel cell, a single controlled prepulse of variable intensity could be obtained by extracting a small portion of the laser intensity before full amplification and having the main pulse pass through a delay line [11,12]. The prepulse to main pulse intensity ratio ranged between 10^{-6} and 10^{-2}; the time difference between the prepulse and the main pulse was 2 or 4.5 ns. Since the main pulse laser intensity on the target was $(1-2)\times10^{13}$ W/cm^2, a prepulse to main pulse intensity ratio of 10^{-6} was considered equivalent to a ''no prepulse'' case as the prepulse intensity was likely then to be below the threshold for preplasma formation.

Figure 1 gives a schematic view of the experimental chamber. The 2-cm long and 150-μm-wide line focus impinged on 2-cm-long solid slab targets of either nickel ($Z=28$), copper ($Z=29$), or zinc ($Z=30$), with an average intensity on target of $(1-2)\times10^{13}$ W/cm^2. The lasing lines were monitored using an axial XUV flat field grazing spectrometer [28] coupled to a time-integrated charge coupled device (CCD) camera or to a streak camera for temporal dispersion. We used a time-integrated x-ray CCD multipinhole camera to image the spectrally integrated keV emission along the plasma line and a potassium acid phtalate (KAP) convex crystal spectrometer coupled to a CCD camera to monitor the ionization of the plasma.

This paper presents results derived from spectra taken with a flat crystal spectrometer (KAP crystal, $2d=26.632$ Å) aimed at the expanding plasma in the horizontal plane of the line focus, 45 ° from its axis. These data are time and space integrated along the density gradient perpendicular to the target plane, but a 50-μm vertical imaging slit provided a 75-μm spatial resolution along the amplification axis. A 25-μm Be filter was positioned in front of the spectrometer slit. The spectra were recorded on Kodak SB-392 film and the conversion from optical density to intensity was done according to Henke *et al.* [29]. More details on the experimental setup have been previously published [11,12].

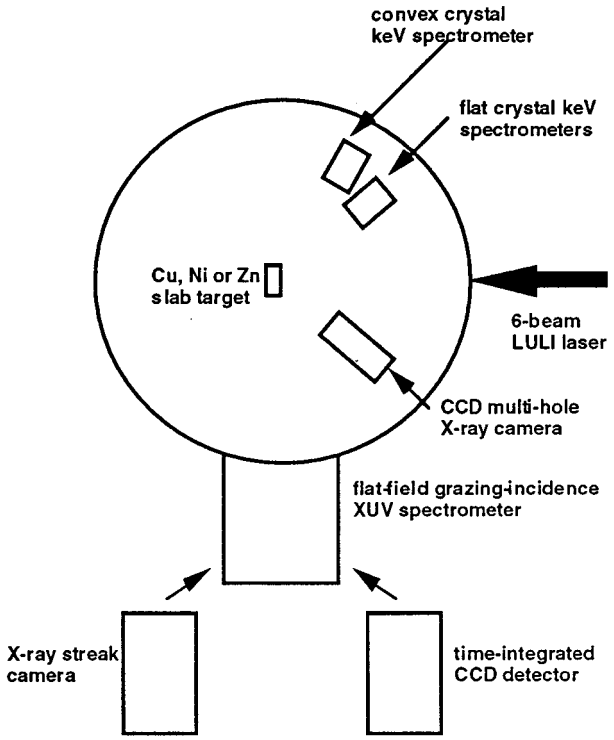

FIG. 1. Schematics of the experimental chamber showing the geometry of the different diagnostics. The flat-field XUV spectrometer could be coupled to either a time-integrated CCD camera or an x-ray streak camera. The data presented in the present paper come from the flat crystal spectrometer (KAP crystal, $2d=26.632$ Å) positioned in the horizontal plane, at 45° from the LULI laser axis.

III. DIAGNOSTICS AND ANALYSIS

It would be useful to summarize here the XUV results obtained during these experiments [11,12]. The intensity of the $J=0-1$ and $J=2-1$ lines of all three x-ray lasers was measured for different single-prepulse intensities (ranging from a prepulse to main pulse ratio of 10^{-6} to 10^{-2}) with variable timing (prepulse arriving 2.0 or 4.5 ns before the main pulse) and with the prepulse train. The $J=0-1$ line of the Zn x-ray laser (at 212 Å) appeared to be the most sensitive to prepulse conditioning (in comparison to the Zn $J=2-1$ line at 267 Å or to the Ni and Cu $J=0-1$ lines at 232 and 221 Å, respectively). This line showed a large increase in intensity when a prepulse was used and even peaked in intensity for a prepulse of about 10^{-3} arriving 4.5 ns before the main pulse; this peak was reproduced in two experimental runs several months apart. The intensities of the $J=0-1$ lines of Ni and Cu did not feature such a peak and increased roughly logarithmically with the prepulse level for the whole range covered. Single prepulses 2.0 ns before the main pulse also increased the output intensity of the lasers but less so than with the 4.5-ns timing. In all cases, the prepulse train gave higher $J=0-1$ x-ray laser intensities than single prepulses. The $J=2-1$ lines in general reacted very little to the addition of prepulses.

Figure 2 shows typical nickel [Fig. 2(a)], copper [Fig. 2(b)], and zinc [Fig. 2(c)] keV spectra taken with the smallest prepulse available (10^{-6}); corresponding records were obtained for all prepulse levels and timing studied. A visual

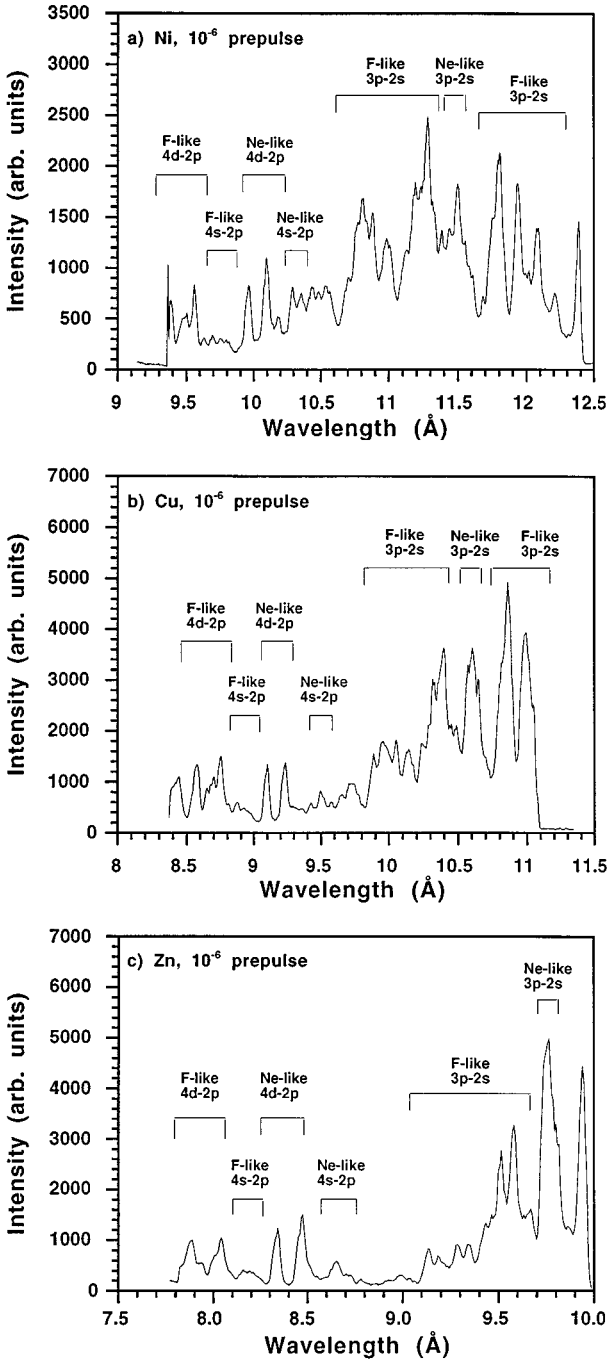

FIG. 2. keV spectra of Ne-like and F-like lines in (a) nickel, (b) copper, and (c) zinc plasmas obtained with the flat crystal spectrometer for the smallest available prepulse and an intensity on target of 1×10^{13} W/cm^2. Results are time integrated and space integrated along the direction perpendicular to the target plane.

inspection of the three spectra indicates a similar ionization balance, with a predominance of 3-2 and 4-2 Ne-like and F-like lines. The spectral resolution is $\approx 150-220$ at 8.34 Å and is mostly limited by the source broadening. It was made to be this low purposefully as we wanted first the spectrometer to be close to the source for reasons of sensitivity and dispersion and second a large source broadening for the Ne-like emission region size diagnostics. Although the spectra are time integrated and averaged over the line of sight, we estimate that these emissions are representative of conditions

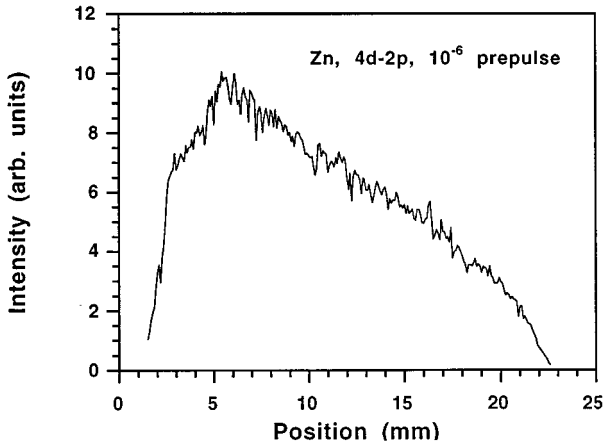

FIG. 3. Spatial profile of the $4d$-$2p$ Ne-like zinc emissions along the line plasma axis, from the spectrum shown in Fig. 2(c).

in the gain region spatial position since they are weighted towards the higher densities ($n_e=10^{20}-10^{21}$ cm^{-3}); temporally, the keV emission is weighted towards the higher temperatures at the maximum of the main laser pulse [20], at the end of the $J=0-1$ lasing time, and at the peak of the $J=2-1$ gain [4,16,17]. Using line ratios of F-like to Ne-like optically thin emissions we deduce the electron temperature T_e of the plasma; with line ratios of optically thin to optically thick Ne-like emissions we obtain values for the Ne-like ground-state density N_g; from the spectral resolution of the spectrometer we derive the lateral (vertical) width of the Ne-like emission zone Δy. All three of these diagnostics are closely related to the $J=0-1$ x-ray laser via the population inversion mechanisms and the propagation of amplified light through the gain region.

As pointed out earlier, we were able to record spatially resolved spectra along the amplification axis. Figure 3 shows the corresponding Zn Ne-like $4d$-$2p$ line intensities and reveals a high degree of inhomogeneity along the axis. The emission is brighter on one side of the line plasma and regularly decreases to the other, this general trend being seen for all the considered Ne-like and F-like lines. We can quantify the homogeneity of the keV emission, closely linked with the performance of collisionally excited x-ray lasers [20,30–33], using its contrast $C=(I_{\max}-I_{\min})/I_{\max}$, where $I_{\max}$ and $I_{\min}$ are, respectively, the maximum and minimum intensities found along the line plasma [31]. From the lineout shown in Fig. 3, we measure a contrast of about 0.75, typical of plasmas produced by lens pairs [31–33]. Such large-scale emission inhomogeneities are in fact the imprint of noticeable variations in the plasma hydrodynamics, mainly due to nonuniformities in the laser energy deposition [20,33]. Hence we can expect to observe corresponding spatial profiles for the plasma parameters of electron temperature and Ne-like ion density.

A. Electron temperature diagnostics

The electron temperature plays a crucial role in the kinetics of the excited levels contributing to the $J=0-1$ inversion, notably the $J=0$ level, which is largely populated through direct collisional excitation from the Ne-like ground

state. It is therefore important to see how, if at all, the plasma electron temperature is affected by the addition of a prepulse to the main driving pulse of the x-ray laser.

The temperature diagnostic is based on the intensity ratio of the optically thin $4s$-$2p$ lines in the Ne-like and F-like ionization stages. These lines were chosen over the more intense $4d$-$2p$ lines because the latter are optically thick and could skew the T_e evaluation from their reabsorption by the plasma [20]. The diagnostics assumes that the $n \geqslant 4$ excited levels of the Ne-like and F-like species are at local thermodynamic equilibrium with the ground state of their next ionization stage the F-like and O-like stages, respectively. Simulations with the hydro–collisional-radiative code EHYBRID [34] and the kinetic code LASIX [35] confirm the validity of this basic hypothesis for line ratio diagnostics. This enables us to use Saha-Boltzmann equations to relate the population N_n^{Z-1} of an excited level n of an ion of charge $Z-1$ to the ground-state population N_1^Z of the next ionization stage:

$$\frac{N_e N_1^Z}{N_n^{Z-1}} = 6.0 \times 10^{21} \frac{g_1^Z T_e^{3/2}}{g_n^{Z-1}} e^{-E_\infty^Z(n)/T_e} \text{ cm}^{-3}, \qquad (1)$$

where g_n^{Z-1} and g_1^Z are the corresponding statistical weights and $E_\infty^Z(n)$ the energy ionization gap between the two involved levels (in eV). For optically thin lines, we can equate the intensity I to the emissivity E:

$$I \approx E = N_u A_{ul} h\nu_{ul}, \qquad (2)$$

where N_u is the upper level population and the A_{ul} the spontaneous-emission coefficient for the transition of energy $h\nu_{ul}$. Combining Eqs. (1) and (2) and substituting in the relevant symbols for the $4s$-$2p$ F-like and $4s$-$2p$ Ne-like emissions, we get an expression for the expected line ratio as a function of the ground-state populations of the F-like and O-like ions and the electron temperature:

$$\frac{I_{4s\text{-}2p}^{\text{F-like}}}{I_{4s\text{-}2p}^{\text{Ne-like}}} = \frac{N_1^{\text{O-like}}}{N_1^{\text{F-like}}} \frac{g_1^{\text{F-like}}}{g_1^{\text{O-like}}} \frac{g_{4s}^{\text{F-like}}}{g_{4s}^{\text{Ne-like}}} \frac{(Ah\nu)_{4s\text{-}2p}^{\text{F-like}}}{(Ah\nu)_{4s\text{-}2p}^{\text{Ne-like}}} \times e^{-[E_\infty^{\text{F-like}}(4s) - E_\infty^{\text{O-like}}(4s)]/T_e}. \qquad (3)$$

Since the recombination time scale is expected to be longer than the hydrodynamic time scale (ionization ''frozen'' in the expansion [36]), the charge-state distribution of the detected emitting region is mostly determined by the ionization conditions at critical density. The dependence of the relevant ionic fractional populations with T_e at critical density were obtained with the detailed configuration accounting (DCA) collisional-radiative model [37,38]. Figure 4 shows a plot versus T_e of the Na-like, Ne-like, F-like, and O-like ground-state populations at a critical density ($n_c = 10^{21}$ cm^{-3}) from DCA simulations for nickel [Fig. 4(a)], copper [Fig. 4(b)], and zinc [Fig. 4(c)]. From these ionization curves and from our earlier observations that Ne-like and F-like emission lines are dominant in the recorded spectra (Fig. 2), we can predict that the electron temperatures should be between 225 and 300 eV for the nickel plasma, between 300 and 375 eV for the copper plasma, and between 350 and 425 eV for the zinc plasma.

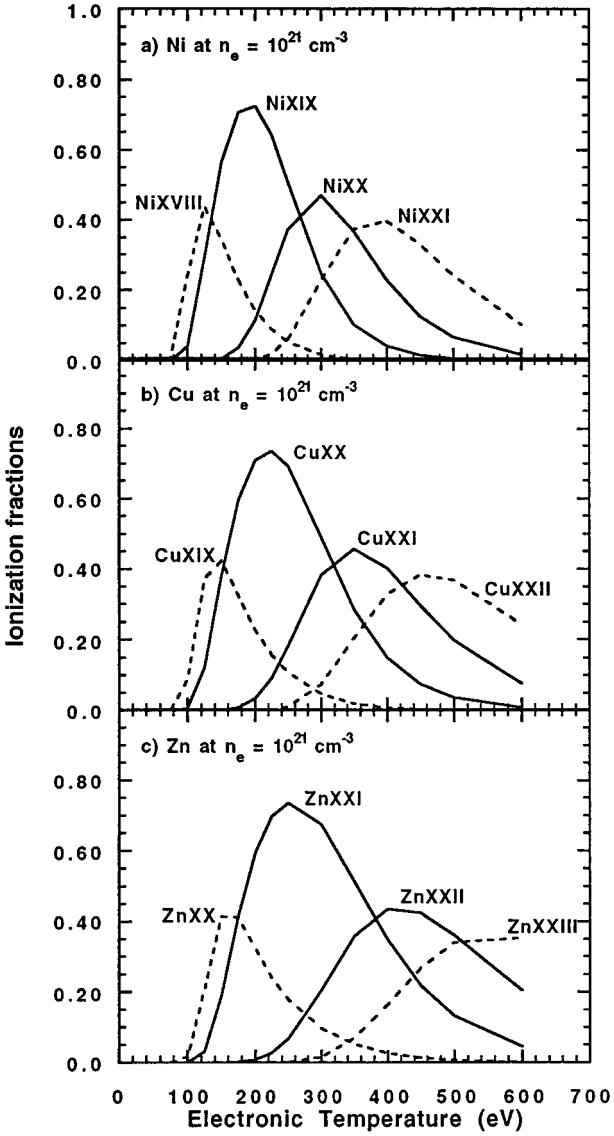

FIG. 4. DCA simulations showing the ionization fractions, in (a) nickel, (b) copper, and (c) zinc plasmas, at an electron density of 10^{21} cm^{-3}, versus electron temperature. For each case, the Na-like, Ne-like, F-like, and O-like fractions are plotted (from left to right, respectively, along the temperature axis).

The multiconfiguration Dirac-Fock (MCDF) code from Grant *et al.* [39] was used to calculate the wavelengths, oscillator strengths, and other atomic data required to solve Eq. (3). Although Eq. (3) is derived here for the ratio of the intensity of *one* F-like $4s$-$2p$ transition to *one* Ne-like $4s$-$2p$ transition, we used in practice the sum of the contributions of several lines of each for a better signal-to-noise figure. For that purpose, we had to use for the energy ionization gap $E_\infty^Z(4s)$, a weighted average over the individual energy ionization gaps for the levels involved in the transitions chosen for the diagnostics. The differences between the individual gaps and the weighted average gaps are on the order of $\pm 3\%$ and thus the use of the weighted average gaps is justified. The deduced line ratio is then plotted in Fig. 5 as a function of the electron temperature for all three cases of nickel, copper, and zinc plasmas. The curves through the data points are fourth-order polynomial fits that were used to

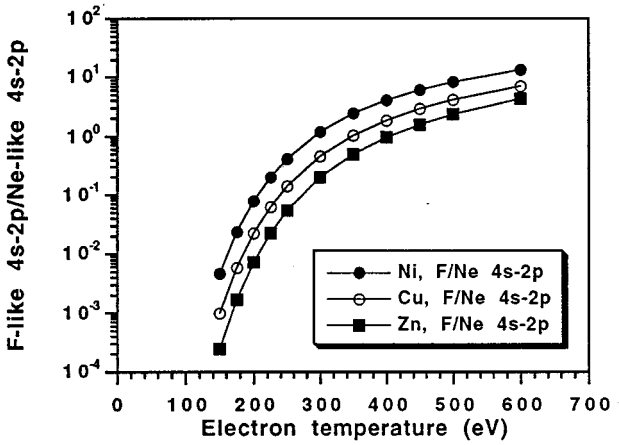

FIG. 5. $4s$-$2p$ F-like to $4s$-$2p$ Ne-like intensity line ratio as a function of electron temperature for nickel, copper, and zinc. The points are calculated with Eq. (3) and DCA simulations from Fig. 4, and are fitted by fourth-order polynomials used to extract the temperature diagnostic from the experimental line ratio.

extract the electron temperature from the experimental line ratios.

Figure 6 shows the T_e values obtained for the zinc plasma as a function of the position along the focus line for three laser shots with different prepulse conditions. One readily notices that the temperature profiles along the amplification axis are slightly nonuniform, presenting the same general shape as the emission profile shown in Fig. 3. The temperature in the hotter zone is about 390 ± 25 eV, which agrees with the rough estimate made earlier. The error bars on the diagnostics arise mostly from the uncertainty on the extraction of the intensity from the data on film, but as can be deduced from Eq. (3), the temperature varies logarithmically with the line ratio and is therefore not too sensitive to this uncertainty; for example, it would take an unlikely error of $\pm 50\%$ on the evaluation of the line ratio to get temperature variations of ± 25 eV. Changing the DCA calculations densities from 8×10^{20} to 1.2×10^{21} cm^{-3} made little difference in the temperature evaluation, and this is included also in the error bars. The temperature, as well as its shape along the line plasma, is seen to remain relatively constant regardless of the prepulse level. We therefore infer that the performance improvement of the x-ray laser using the prepulse technique is likely not due to a change of the temperature (which could have arisen from a better coupling of the main pulse energy to the target in presence of a preplasma) or from a large-scale smoothing of the temperature profile along the amplification axis; possible small-scale smoothing (< 50 μm) could not be detected with the present spatial resolution along the line plasma. However, this last statement has to be viewed in light of the fact that the diagnostics gives the temperature at the peak of the laser pulse, which is slightly after the peak of the $J=0-1$ gain [4,16,17]. In order to verify that the temperature is unchanged with the prepulse level at the time of maximum $J=0-1$ gain, one would have to couple the spectrometer to a streak camera. For copper and nickel plasmas, the temperature profiles are quite similar to those shown in Fig. 6, but show maxima of 335 ± 25 and 250 ± 25 eV, respectively. According to the DCA results (Fig. 4), these diagnosed electron temperatures, for all three cases of zinc,

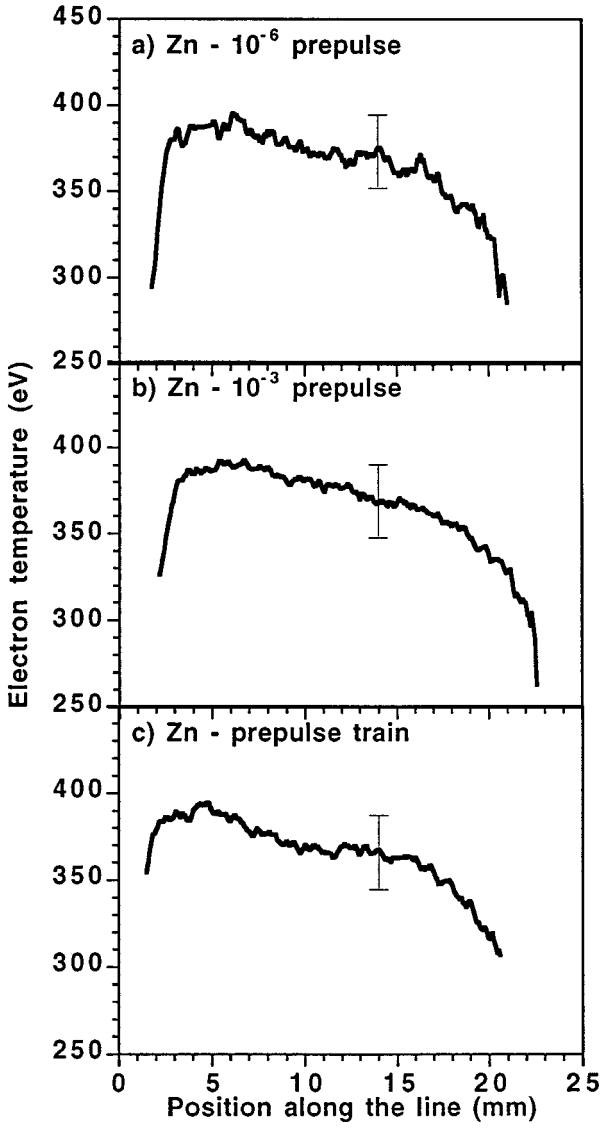

FIG. 6. Zinc plasma electron temperature, as a function of the position along the focus line, derived from the $4s$-$2p$ F-like to $4s$-$2p$ Ne-like intensity line ratios, for three cases of prepulse to main pulse intensity contrasts: (a) 10^{-6} prepulse, (b) 10^{-3} prepulse, and (c) prepulse train.

copper, and nickel plasmas, correspond to an ionization balance of approximately equal proportions of Ne-like and F-like ions, close to ideal for the achievement of high $J=0-1$ gain. The fact that the electron temperature is constant for any given target material within the prepulse range surveyed and that it increases when the target changes from Ni to Cu to Zn is mirrored in our CHIVAS-LASIX simulations, which show a similar behavior of the temperature of the plasma near critical density, at the maximum of the laser pulse (see Sec. III D).

B. Ne-like lateral source size diagnostics

Another important issue for the $J=0-1$ x-ray laser is the ability of the XUV radiation to propagate through the amplifying medium. The more of the gain region the ray trajectories sample, the higher the integrated gain coefficient and

output intensity. Part of the reason why the $J=2-1$ lasers were originally more successful than the $J=0-1$ one is that the latter has a smaller gain region, closer to the target. This means that the $J=0-1$ x rays went through much higher density gradients and deviated outside the gain region before having passed the full length of the plasma column. Along with the much-studied density gradients *perpendicular* to the target plane, there are important *lateral* density gradients, which also tend to make the x-ray laser beam exit the gain region before traveling the whole length of the plasma [21,22]. Here we address how the prepulsed irradiation affects the lateral width of the gain region.

As our keV spectrometer featured a vertical slit to allow for spatial resolution along the amplification axis, any given point on the crystal could ''see'' the whole vertical width of the line plasma. Hence a region of the plasma emitting at wavelength λ subtended an angle $\Delta\theta$ around the Bragg angle θ_B for that wavelength on the crystal. This finite angular spread of the source induced a broadening $\Delta\lambda$ of the spectral line on film. The lateral (vertical) width Δy of the emitting regions in the plasma can then be determined through the spectral width of the emission lines via the well-known expression [40]

$$\Delta y = L\sqrt{\left(\frac{\Delta\lambda}{\lambda}\right)^2 \tan^2\theta_B - (\Delta\theta_c)^2}, \tag{4}$$

where L is the distance of the source to the crystal, $\Delta\lambda/\lambda$ the spectral resolution of film, and θ_B and $\Delta\theta_c$ the Bragg angle and the crystal rocking curve for the wavelength λ. We had positioned the spectrometer close enough to the plasma to measure by that method the Ne-like source size from the $4d$-$2p$ Ne-like lines.

Figure 7 shows the deduced Ne-like region lateral size as a function of the single prepulse level and for the prepulse train, for the cases of nickel [Fig. 7(a)], copper [Fig. 7(b)], and zinc [Fig. 7(c)]; the widths were taken in the hotter zone along the line plasma. The circles and squares represent data taken with prepulses 4.5 and 2.0 ns, respectively, before the main pulse. The prepulse train cannot be easily compared (in terms of level and delay) to the single prepulses and it is conveniently represented by bars starting at 5×10^{-4}. The straight lines drawn through the data points are fits, suggesting that the lateral size of the Ne-like region increases roughly logarithmically with the prepulse level for all the three x-ray laser plasmas. The prepulse train, which gives the highest $J=0-1$ intensity in the axial XUV spectrometer, also shows the largest increase in Ne-like lateral source size, with Ne-like regions 35% and 60% wider over the smallest prepulse cases in copper and zinc, respectively. It is the zinc plasma that shows by far the largest increase in Ne-like lateral source size, which correlates well with the observed XUV results, which give a better improvement for the zinc $J=0-1$ laser than for the copper or nickel $J=0-1$ lasers with the use of the prepulse. The noticeable lateral size increase of the Ne-like region for the cases of the prepulse train and single prepulses 4.5 ns before the main pulse is not as evident for the case of the prepulses 2.0 ns before the main pulse. These data are only available for nickel and zinc. The preplasma created by the prepulse seems not to have enough time to expand sufficiently during the 2.0 ns to show

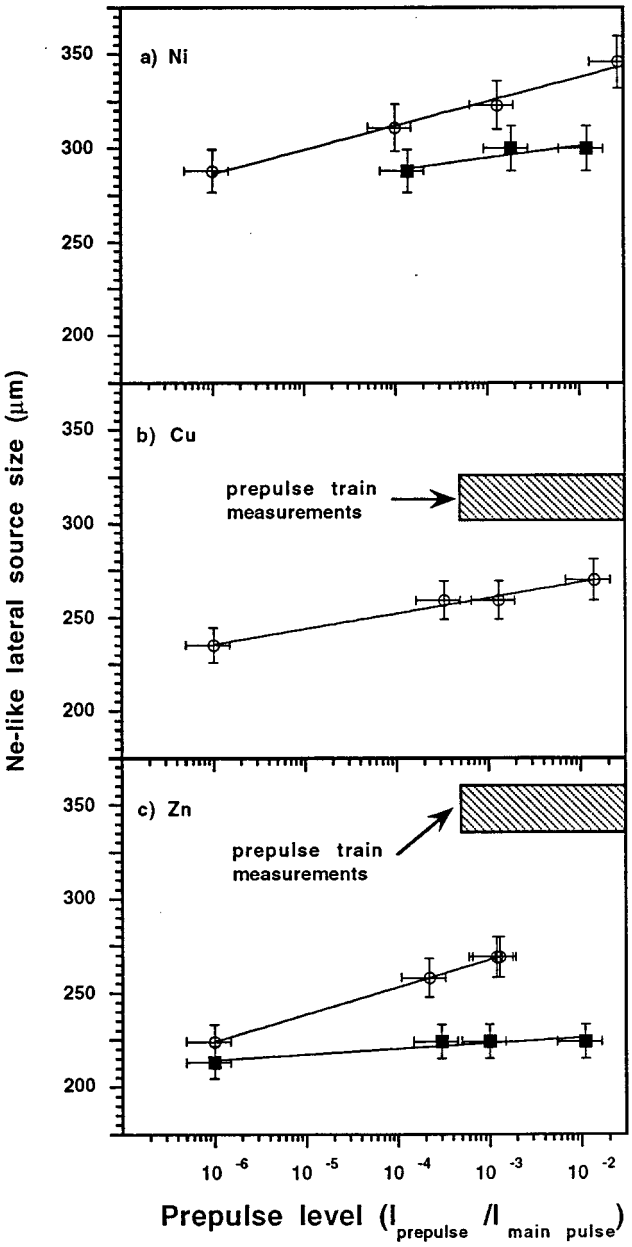

FIG. 7. Dependence of the Ne-like lateral source size on the prepulse level for (a) nickel, (b) copper, and (c) zinc plasmas, derived from the spectral resolution on the Ne-like $4d$-$2p$ lines. Circles and squares are for data with a prepulse 4.5 and 2.0 ns before the main pulse, respectively; the prepulse train effective level is represented by the shaded bar. Measurements are taken in the hotter region of the plasma (see Fig. 6). The lines are logarithmic fits through the single prepulse data.

a marked difference on the spectra of the keV emission observed during the main pulse. The XUV records show correspondingly that the $J=0-1$ line of zinc, copper, and nickel display larger increases in intensity when the 4.5-ns prepulse is used over the 2.0-ns prepulse case [11,12].

This sizable increase in the lateral width of the Ne-like region in the plasma can play a determinant role towards explaining the better performance of x-ray lasers when prepulses are used. Both a reduction of the density gradient steepness and a more extended gain region could reduce the

propagation problem; also, a larger gain region gives a larger source to seed the amplification [21–24]. Our ongoing work on numerical simulations including propagation effects will help determine just how much of an influence on the x-ray laser output the increase in lateral size may have. Furthermore, although this diagnostic cannot measure it, it could be reasonably argued that there is a quite comparable increase in the Ne-like region in the direction of the expansion perpendicular to the target [22]. The changes in Ne-like region size and in the density gradients perpendicular to the target may yet be responsible for most of the increased performances of x-ray lasers with prepulses [10].

C. Ne-like ground-state density diagnostics

Since the $J=0$ upper state of the x-ray laser is mainly populated through direct collisional excitation from the Ne-like ground state, those ground-state ions constitute the x-ray laser's pump reservoir. For that reason, we chose to look at the effect of the prepulse level on the Ne-like density in the lasing plasma.

Because our spectrometer was in the horizontal plane of the linear focus axis and aimed at the plasma with a 45° angle, the keV emission detected on film was integrated along the line of sight through the expanding plasma and reabsorption processes have to be taken into account. The detected intensity I is reduced from its original optically thin value I_0 such that $I=I_0\exp(-\tau)$, where τ is the opacity of the plasma. For a Doppler-broadened emission line in a static homogeneous plasma, the latter is related to the absorbing ion density N_g (in cm^{-3}) and to the distance traveled in the absorbing medium d (in cm) as

$$\tau = 1.1\times 10^{-16}\lambda_c N_g d f_{\mathrm{osc}} \sqrt{\frac{M}{T_i}}, \tag{5}$$

where λ_c is the wavelength of the reabsorbed photons at the center of the studied line (in Å), f_{osc} the absorption oscillator strength, T_i the ion temperature of the plasma (in eV), and M the atomic mass number [14]. Thus, for resonant transitions from the same ionization stage, the detected emergent intensity ratio of an optically thin line to an optically thick one can be linked to the ground-state density through their respective opacities. Using the optically thin Ne-like $4s$-$2p$ ($\tau\approx 0.5$) and optically thick Ne-like $4d$-$2p$ ($\tau\approx 14$) emissions, we can determine the quantity of reabsorbing Ne-like material $N_g d$ in the line of sight of the spectrometer, from the line intensity ratio

$$\left(\frac{I_{4s\text{-}2p}}{I_{4d\text{-}2p}}\right)=\left(\frac{I_{4s\text{-}2p}}{I_{4d\text{-}2p}}\right)_{\mathrm{calc}} \exp\left(-1.1\times 10^{-16}\sqrt{\frac{M}{T_i}}N_g d \times\left[(\lambda_c f_{\mathrm{osc}})_{4s\text{-}2p}-(\lambda_c f_{\mathrm{osc}})_{4d\text{-}2p}\right]\right), \tag{6}$$

where the first multiplicative term on the right-hand side is the emissivity ratio calculated using MCDF data and a Boltzmann distribution between the $4s$ and $4d$ upper levels [Eq. (2)]. Since the spectrometer was looking into a nonhomogeneous expanding plasma, a more realistic prescription for the opacity will include the Sobolev escape probability [41].

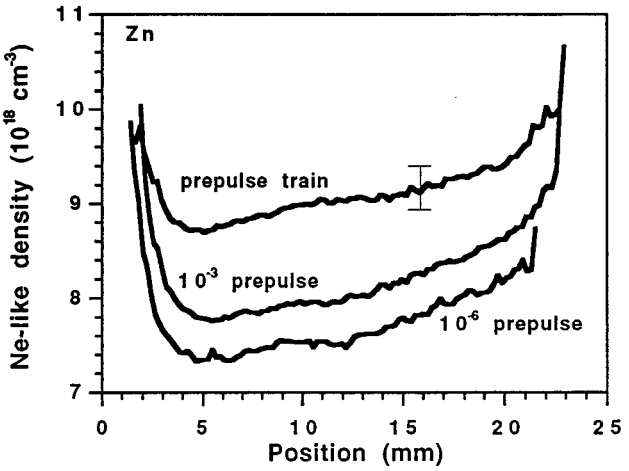

FIG. 8. Zinc Ne-like ground-state density as a function of the position along the line plasma, for three cases of prepulse to main pulse intensity contrasts. The values are averaged over the line of sight of the spectrometer as derived from the $4s$-$2p$ to $4d$-$2p$ Ne-like intensity line ratios.

This can be done by replacing $(2T_i/M)^{1/2}/d$ in the previous expression by the velocity gradient $(\Delta v/\Delta z)$ [14]. Assuming a self-similar expansion ($\Delta v/\Delta z=\alpha/t$, where α is a proportionality constant and t and considered time, in ns [36]), Eq. (6) becomes

$$\left(\frac{I_{4s\text{-}2p}}{I_{4d\text{-}2p}}\right)=\left(\frac{I_{4s\text{-}2p}}{I_{4d\text{-}2p}}\right)_{\mathrm{calc}} \exp\left(-1.1\times 10^{-10}\frac{\sqrt{2}N_g}{(\Delta v/\Delta z)\cos^2\theta} \times\left[(\lambda_c f_{\mathrm{osc}})_{4s\text{-}2p}-(\lambda_c f_{\mathrm{osc}})_{4d\text{-}2p}\right]\right), \tag{7}$$

where the $\cos^2\theta$ factor takes into account the 45° angle the line of sight makes with the velocity gradient perpendicular to the target. By isolating N_g from the rest of Eq. (7), we can evaluate the average Ne-like ground-state density of the plasma in the line of sight directly from the experimental line ratio. This expression is derived for the case of the ratio of single lines, but as was the case for the electron temperature diagnostic described in Sec. III A, we used the ratio of several lines for the Ne-like density diagnostic (two $4s$-$2p$ lines and two $4d$-$2p$ lines). This leads to a slight systematic underestimation in the derived average Ne-like density of less than 5%. Our CHIVAS-LASIX hydrodynamics simulations for zinc confirm that the use in Eq. (7) of a velocity gradient independent of the prepulse level is justified. Because nickel, copper, and zinc are elements of similar atomic number, we make the further assumption that the velocity gradients are the same for the three elements; detailed simulations on Ni and Cu would be needed to validate this assumption.

Figure 8 shows the average Ne-like ground-state density profiles for the case of zinc plasmas created with various prepulse conditions (the corresponding temperature profiles being given on Fig. 6). Whereas no change in temperature was observed, there is a clear increase in the Ne-like ground-state density with increasing prepulse level, from 10^{-6} through 10^{-3} and to the prepulse train. The profiles shown in Fig. 8 give lower densities in the hotter zone (at 390 eV on

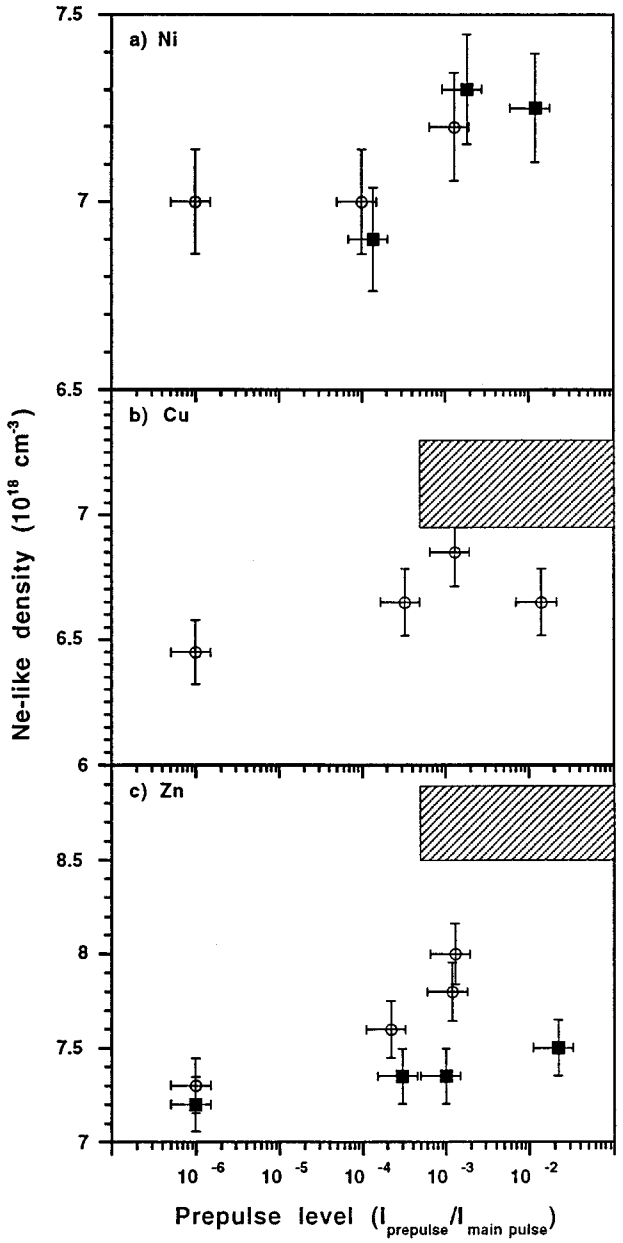

FIG. 9. Dependence of the average density of Ne-like material in the line of sight of the spectrometer on the prepulse level for (a) nickel, (b) copper, and (c) zinc, derived from the $4s$-$2p$ to $4d$-$2p$ Ne-like intensity line ratios. Circles and squares are for data with a prepulse 4.5 and 2.0 ns before the main pulse, respectively; the prepulse train effective level is represented by the shaded bar. Measurements are taken in the hotter region of the plasma (see Fig. 6).

Fig. 6) with an increase towards the cooler part of the line plasma (at 320 eV). Similarly, going back to the zinc ionization curves [Fig. 4(c)], we notice that the Ne-like fraction in the plasma increases as the temperature falls from 390 to 320 eV. Since the two diagnostics are independent, this qualitative agreement shows an important self-consistency. Figure 9 gives the value of the Ne-like ground-state density (taken in the hotter zone along the line plasma axis) as a function of the prepulse level, for the cases of nickel [Fig. 9(a)], copper [Fig. 9(b)], and zinc plasmas [Fig. 9(c)]; the legend for the data points has been given for Fig. 7. For all three cases, the average Ne-like ground-state density increases with the prepulse, though the changes in density are less impressive than the changes in Ne-like source size shown in Fig. 7. The nickel, copper, and zinc plasmas show variations in Ne-like ground-state density of 3%, 10%, and 20%, respectively, from the lowest prepulse level to the prepulse train case (or to the highest single-prepulse case for Ni). The difference between using a prepulse 2.0 or 4.5 ns before the main pulse is unclear in the case of nickel, but for the zinc laser, it seems that the longer delay enables the creation of a denser Ne-like region. The vertical error bars on Fig. 9 take into account the uncertainty in measuring the line ratios from the experimental data but not the systematic underestimation of less than 5% due to the use of several lines in the intensity ratios. Also not included in the error bars is the error due to the value of the chosen velocity gradient. Although reasonable values were used for α and t ($\alpha=1.75$, $t=0.6$ ns [42]), the absolute values for N_g on the vertical axis could change by as much as a factor of 2 either way, depending on the choice of these parameters; this does not, however, affect the observed relative changes in the Ne-like ground-state density, which is what is of importance here.

This higher density of ions, directly available to pump the $J=0$ level, could lend itself as a partial explanation for the better performance of the $J=0-1$ x-ray laser when using the prepulse irradiation. The population inversion would be more efficiently pumped, leading to an overall higher lasing intensity. These increases in Ne-like density are rather small, but they are ordered the same way as the Ne-like region size increases, nickel having the smallest and zinc the largest. This trend in both diagnostics is mirrored by the x-ray laser intensity measurements, which indicate that the $J=0-1$ zinc laser is the most positively affected by the use of a prepulse. A reason for the relatively small changes of the Ne-like density given by this diagnostic is that this method gives only the value of N_g averaged over the whole line of sight of the spectrometer. It can be reasonably argued that spatial resolution along the plasma expansion could reveal more important variations of N_g with the prepulse level in the zones nearer the target.

D. Comparison to CHIVAS-LASIX simulations

The spectroscopic diagnostics presented and discussed in Secs. III A–III C point to measurable changes in the plasma parameters when prepulses are used. Recent postprocessed 1D 1/2 hydrodynamics simulations [22,24] show similar trends. A complete discussion on the theoretical results obtained with the CHIVAS-LASIX-SPECTRA codes are planned to be presented in a later paper, but we show in Table I calculated electron temperatures, Ne-like lateral widths, and Ne-like densities for particular cases relevant to the experimental results presented above. These ''observables'' were obtained from line ratios using artificial spectra generated by postprocessing the CHIVAS-hydrodynamics–LASIX-detailed-kinetics simulations with the SPECTRA radiative transfer code. The SPECTRA simulations took into account the experimental detection geometry of the spectrometer. All the simulation results in Table I are for zinc plasmas.

The calculated electron temperature ($T_e \approx 335$ eV) agrees well with the range of temperatures seen along the line plasma for the cases shown in Fig. 6 (''no prepulse'' in the

TABLE I. Results from CHIVAS-LASIX-SPECTRA simulations for a Zn plasma, irradiated by a 1.06-μm, 800-ps FWHM Gaussian pulse at 2×10^{13} W/cm^2 (the width of the focus line being 150 μm). The values for the electron temperature, lateral width, and Ne-like density were obtained via line ratios of the artificial spectra using the same diagnostics as for the experimental cases.

Prepulse conditions [$I_{\text{prepulse}}/I_{\text{main}}$, delay (ns)]	Electron temperature (eV)	Lateral width Ne-like region (μm)	Ne-like ion density (cm^{-3})
no prepulse	336	244	5.0×10^{18}
10^{-4}, -4.5	336	244	5.0×10^{18}
10^{-3}, -4.5	338	252	5.2×10^{18}
10^{-2}, -4.5	346	290	6.7×10^{18}
10^{-1}, -4.5	380	468	1.0×10^{19}
10^{0}, -4.5	378	722	1.0×10^{19}
prepulse train	333	260	5.9×10^{19}
10^{-2}, -2.0	335	256	5.3×10^{19}

simulations is equivalent to a 10^{-6} prepulse in the experiment). The insensitivity of the experimentally measured electron temperature to the prepulse level (Fig. 6) is reproduced in our simulations, the constant T_e value being set by the intensity of the main pulse within the range of prepulses surveyed in the present experiment. There are some indications in the simulations that in fact the temperature of the plasma during the main pulse could increase for very high prepulse levels (prepulse to main pulse intensity ratios of 0.1 to 1) not covered in the experiments. Regardless, our prepulsed x-ray laser experiments show large $J=0-1$ intensity increases with prepulse levels as low as 10^{-3} and 10^{-2}, where the temperature remains constant.

The values of the Ne-like lateral size Δy calculated from the simulations correspond very well with those presented in Fig. 7(c), except for the case of the prepulse train, which shows a smaller increase in the simulations. This difference in calculated and measured widths for the prepulse train case may be due to the fact that the simulations consider only three prepulses in the train, instead of the five or more present in the real laser pulse.

Finally, the last column in Table I gives the mean values of the Ne-like density for the different prepulse conditions. As with the experimental diagnostics, the density increase slightly with the prepulse level. The calculated values are in general lower than those obtained from the experimental spectra, but that is likely due to the velocity gradient chosen to evaluate the latter. As noted in Sec. III C above, the value of the velocity gradient used in the experimental diagnostics was reasonable within a factor of 2.

IV. SUMMARY AND CONCLUSIONS

In order to establish why $J=0-1$ Ne-like collisional x-ray lasers show dramatic improvements in performance when prepulses are used, we have conducted a quantitative experimental characterization of x-ray laser plasmas created using the prepulse technique. The three x-ray lasers we studied particularly are the nickel, copper, and zinc lasers, with $J=0-1$ lines at 232, 221, and 212 Å, respectively. The prepulse parameter space included single prepulses either 2.0 or 4.5 ns before the main pulse, with intensities ranging from 10^{-6} to 10^{-2} of that of the main pulse, and a prepulse train with an effective level of 5×10^{-4} or more. Although the keV spectroscopy data are time integrated and averaged over the line of sight of the spectrometer, we expect that the recorded emissions used for this analysis originate mostly from regions relevant to the amplification since they are weighted towards the higher densities ($n_e=10^{20}-10^{21}$ cm^{-3}); temporally, the keV emission is weighted towards the higher temperatures at the maximum of the main laser pulse [20], at the end of the $J=0-1$ lasing time, and at the peak of the $J=2-1$ gain [4,16,17].

We observed that the plasma temperature and large-scale uniformity along the line focus are unchanged by varying the prepulse level, thereby concluding that the improvement in x-ray laser performances does not come principally from a possible change in these parameters. The lateral size of the Ne-like region is seen to increase with the prepulse level, which could contribute to better the x-ray laser efficiency in two ways: first, by providing a larger amplification area and, second, by allowing the XUV rays to sample a longer gain region before being refracted out of it. We obtain that the Ne-like ground-state density in the plasma also increases (albeit marginally) with the prepulse level, which should tend to create a more efficient pumping of the $J=0$ upper level through direct collisional excitation from the Ne-like ground state. All in all, a larger and denser Ne-like region in the plasma will contribute to augment the integrated gain and intensity output of the $J=0-1$ line, which could explain in part the positive effect on that line given by the use of a prepulse technique. The diagnostics are in good agreement with our recent CHIVAS-LASIX-SPECTRA simulations, which reproduce very well the experimental results. Other aspects of our ongoing simulation work will help determine how much of the x-ray laser improvements with prepulsed irradiation is due to the lateral size enhancement and the Ne-like density increase; undoubtedly, the smoothing of the density gradients perpendicular to the target also plays a crucial role, and one could argue that most of the improvements come from there. Hence it is not altogether surprising that the $J=2-1$ lines are seen to react less dramatically to the prepulses, as they are emitted at a later time, in a more extended region farther from the target: they are thus less sensitive to eventual smoothings of the density gradients and to

an increase in the plasma size near the target.

It is difficult to ascertain from the results presented here if a prepulse train is more favorable to the $J=0-1$ lasing than a single prepulse. The difference seen in the present work may be due simply to the larger time delay between the last prepulse of the train and the main pulse; we observed smaller improvements of the x-ray laser performance when a delay of 2.0 ns was used for the single prepulse instead of 4.5 ns, which would support this last hypothesis [11,12]. Further single prepulse experiments with longer delays would help answer this question. Also, the keV results presented here cannot account for the observed ''peak'' of XUV emission for prepulses of level 10^{-3} in the zinc $J=0-1$ x-ray laser. That this peak was observed only for the case of zinc in our XUV results raises questions about a possible effect of the solid-state aspect of the target. For example, zinc has melting and vaporizing latent heat 2–4 times lower that those of copper and nickel, which could play a significant role in the effect of the prepulse on target conditioning. Other aspects that could not be studied here but should be the focus of other experiments concern the density gradients and the Ne-like region extension perpendicular to the target; to study the dynamics of the parameters involved, the use of an x-ray streak camera for temporal dispersion would then be crucial.

ACKNOWLEDGMENTS

The authors would like to thank P. Goedtkindt, M. Holden, and J. Krishnan, as well as J. C. Lagron and L. Vanbostal from LSAI, for their help in the design and construction of the spectrometer used in this study. We would also like to thank the laser staff at LULI for implementing the delay line for the controlled prepulse creation. We are indebted to C. Y. Côté, J. C. Kieffer, and J. P. Matte from INRS-Energie et Matériaux, Varennes, Québec for the DCA simulations. Finally, we would like to acknowledge fruitful discussions with A. Sureau. This work has been supported by EC through the HCM, under Contract No. CHGECT390046.

[1] *X-Ray Lasers 1994*, edited by D. Eder and D. Matthews, AIP Conf. Proc. No. 332 (AIP, New York, 1995), p. 289.

[2] T. Boehly, M. Russotto, R. S. Craxton, R. Epstein, B. Yaakobi, L. B. Da Silva, J. Nilsen, E. A. Chandler, D. J. Fields, B. J. MacGowan, D. L. Matthews, J. H. Scofield, and G. Shimkaveg, Phys. Rev. A **42**, 6962 (1990).

[3] J. Nilsen, B. J. MacGowan, L. B. Da Silva, and J. C. Moreno, Phys. Rev. A **48**, 4682 (1993).

[4] J. Nilsen, J. C. Moreno, B. J. MacGowan, and J. A. Koch, Appl. Phys. **57B**, 309 (1993).

[5] J. Nilsen and J. C. Moreno, Opt. Lett. **19**, 1137 (1994).

[6] G. F. Cairns, M. J. Lamb, C. L. S. Lewis, A. G. MacPhee, D. Neely, P. Norreys, M. H. Key, C. Smith, S. B. Healy, P. B. Holden, G. Pert, and J. A. Plowes, Soft X-ray Lasers and Applications, edited by J. J. Rocca and P. L. Hagelstein SPIE Proc. No. 2520 (SPIE, Washington, D.C., 1995).

[7] P. Jaeglé, A. Carillon, P. Dhez, P. Goedtkindt, G. Jamelot, A. Klisnick, B. Rus, P. Zeitoun, S. Jacquemot, D. Mazataud, A. Mens, and J. P. Chauvineau, in *Atomic Processes* (Ref. [6]), p. 25.

[8] E. E. Fill, Y. Li, D. Schlögl, J. Steingruber, and J. Nilsen, Opt. Lett. **20**, 374 (1995).

[9] Y. Li, G. Pretzler, and E. E. Fill, Phys. Rev. A **51**, R4341 (1995).

[10] Y. Li, G. Pretzler, and E. E. Fill, Phys. Rev. A **52**, R3433 (1995); Y. Li, G. Pretzler, E. E. Fill, and J. Nilsen, J. Opt. Soc. Am. B **13**, 742 (1996).

[11] G. Jamelot, P. Jaeglé, B. Rus, A. Carillon, A. Klisnick, M. Nantel, S. Sebban, F. Albert, P. Zeitoun, E. Plankl, A. Sirgand, C. L. S. Lewis, A. MacPhee, G. J. Tallents, J. Krishnan, and M. Holden, SPIE Proc. **2520**, 2 (1995).

[12] G. J. Tallents, P. Zeitoun, A. Behjat, A. Demir, M. Holden, J. Krishnan, C. L. S. Lewis, A. MacPhee, P. J. Warwick, M. Nantel, G. Jamelot, B. Rus, P. Jaeglé, A. Klisnick, P. Goedtkindt, A. Carillon, E. E. Fill, Y. Li, G. Pretzler, D. Shlögl, J. Steingruber, D. Neely, P. Norreys, M. H. Key, J. Zhang, G. J. Pert, S. B. Healy, and J. Plowes, SPIE Proc. **2520**, 34 (1995); A. G. MacPhee, C. L. S. Lewis, P. J. Warwick, I. Weaver, P. Jaeglé, A. Carillon, G. Jamelot, A. Klisnick, B. Rus, Ph. Zeitoun, M. Nantel, P. Goedtkindt, S. Sebban, G. J. Tallents, A. Demir, M. Holden, and J. Krishnan, (to be published).

[13] B. Rus, Ph.D. thesis, Université de Paris–Sud, 1995 (unpublished).

[14] R. C. Elton, *X-Ray Lasers* (Academic, New York, 1990), and references therein.

[15] M. D. Rosen, P. L. Hagelstein, D. L. Matthews, E. M. Campbell, A. U. Hazi, B. L. Whitten, B. J. MacGowan, R. E. Turner, and R. W. Lee, Phys. Rev. Lett. **54**, 106 (1985).

[16] B. Rus, A. Carillon, B. Gauthé, P. Goedtkindt, P. Jaeglé, G. Jamelot, A. Klisnick, A. Sureau, and P. Zeitoun, J. Opt. Soc. Am. B **11**, 564 (1994).

[17] B. Rus, A. Carillon, P. Dhez, B. Gauthé, P. Goedtkindt, P. Jaeglé, G. Jamelot, A. Klisnick, M. Nantel, A. Sureau, and P. Zeitoun, in *Atomic Processes* (Ref. [6]), p. 152.

[18] R. A. London, Phys. Fluids **31**, 184 (1988).

[19] M. D. Rosen, Phys. Fluids B **2**, 1461 (1990).

[20] B. La Fontaine, J. Dunn, H. A. Baldis, G. D. Enright, D. M. Villeneuve, J. C. Kieffer, M. Nantel, and H. Pépin, Phys. Rev. E **47**, 583 (1993).

[21] J. A. Plowes, G. J. Pert, and P. B. Holden, Opt. Commun. **117**, 189 (1995).

[22] P. B. Holden and B. Rus, Opt. Commun. **119**, 424 (1995).

[23] S. Jacquemot, in *Atomic Processes* (Ref. [6]), p. 279.

[24] S. Jacquemot and L. Bonnet, SPIE Proc. **2520**, 169 (1995).

[25] Ph. Zeitoun *et al.* (unpublished).

[26] T. Mocek, B. Rus, M. Kalal, P. Zeitoun, A. Demir, G. Jamelot, B. Kralikova, J. Krasa, L. Pina, S. Sebban, J. Skala, and G. J. Tallents, SPIE Proc. (to be published).

[27] M. Nantel, A. Klisnick, G. Jamelot, P. B. Holden, P. Jaeglé, P. Zeitoun, G. Tallents, A. G. MacPhee, and C. L. S. Lewis, Opt. Lett. **20**, 2333 (1995).

[28] T. Harada and T. Kita, Appl. Opt. **19**, 3987 (1980).

[29] B. L. Henke, J. Y. Uejio, G. F. Stone, C. H. Dittmore, and F. G. Fujiwara, J. Opt. Soc. Am. B **3**, 1540 (1986).
[30] T. N. Lee, W. A. Molander, J. L. Ford, and R. C. Elton, Rev. Sci. Instrum. **57**, 2052 (1986).
[31] J. C. Kieffer, M. Chaker, H. Pépin, M. Nantel, H. A. Baldis, J. Dunn, G. D. Enright, and D. M. Villeneuve, Opt. Commun. **84**, 208 (1991).
[32] M. Nantel, J. C. Kieffer, B. La Fontaine, H. Pépin, G. D. Enright, D. M. Villeneuve, J. Dunn, H. A. Baldis, and O. Peyrusse, Phys. Fluids **5**, 4465 (1993).
[33] M. Nantel, J. C. Kieffer, G. D. Enright, D. M. Villeneuve, J. Dunn, A. S. Wan, R. S. Walling, H. Scott, A. Osterheld, and O. Peyrusse, J. Phys. B **28**, 2765 (1995).
[34] P. B. Holden, S. B. Healy, M. T. M. Lightbody, G. J. Pert, J. A. Plowes, A. E. Kingston, E. Robertson, C. L. S. Lewis, and D. Neely, J. Phys. B **27**, 341 (1994).
[35] S. Jacquemot and A. Decoster, Laser Part. Beams **9**, 517 (1991).
[36] R. A. London and M. D. Rosen, Phys. Fluids **29**, 3813 (1986).
[37] Y. T. Lee, J. Quant. Spectrosc. Radiat. Transfer **38**, 131 (1987).
[38] C. Y. Côté, J. C. Kieffer, and J. P. Matte (private communication).
[39] I. P. Grant, B. J. McKenzie, P. H. Norrington, D. P. Mayers, and N. C. Pyper, Comput. Phys. Commun. **21**, 207 (1980).
[40] A. A. Hauer, N. D. Delamater, and Z. M. Koenig, Laser Part. Beams **9**, 3 (1991).
[41] V. V. Sobolev, Sov. Astron. Astrophys. J. **1**, 678 (1957).
[42] M. Nantel, Ph.D. thesis, Université du Québec, 1994 (unpublished).